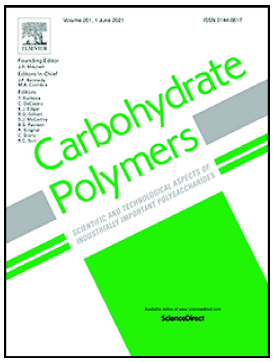

Enzymatic production of xylooligosaccharides from corn cobs: Assessment of two different pretreatment strategies

Caio Cesar de Mello Capetti, Vanessa de Oliveira Arnoldi Pellegrini, Melissa Cristina do Espirito Santo, Anelyse Abreu Cortez, Maurício Falvo, Antonio Aprigio da Silva Curvelo, Eleonora Campos, Jefferson Gonçalves Filgueiras, Francisco Eduardo Gontijo Guimaraes, Eduardo Ribeiro de Azevedo, Igor Polikarpov

PII: S0144-8617(22)01079-7

DOI: https://doi.org/10.1016/j.carbpol.2022.120174

Reference: CARP 120174

To appear in: *Carbohydrate Polymers*

Received date: 3 July 2022

Revised date: 23 September 2022

Accepted date: 26 September 2022

Please cite this article as: C.C. de Mello Capetti, V. de Oliveira Arnoldi Pellegrini, M.C. do Espirito Santo, et al., Enzymatic production of xylooligosaccharides from corn cobs: Assessment of two different pretreatment strategies, *Carbohydrate Polymers* (2022), https://doi.org/10.1016/j.carbpol.2022.120174

Enzymatic production of xylooligosaccharides from corn cobs: Assessment of two different pretreatment strategies

Caio Cesar de Mello Capetti[1], Vanessa de Oliveira Arnoldi Pellegrini[1], Melissa Cristina do Espirito Santo[1], Anelyse Abreu Cortez[1], Maurício Falvo[1], Antonio Aprigio da Silva Curvelo[2], Eleonora Campos[3,4], Jefferson Gonçalves Filgueiras[5,6], Francisco Eduardo Gontijo Guimaraes[1], Eduardo Ribeiro deAzevedo[1] and Igor Polikarpov[1]*

[1] Instituto de Física de São Carlos, Universidade de São Paulo, Avenida Trabalhador São-carlense 400, 13566-590 São Carlos, SP, Brazil.

[2] Instituto de Química de São Carlos, Universidade de São Paulo, Avenida Trabalhador São-carlense 400, 13566-590 São Carlos, SP, Brazil.

[3] Instituto de Biotecnología, CICVyA, Instituto Nacional de Tecnología Agropecuaria (INTA), Los Reseros y N. Repetto, Hurlingham B1686, Buenos Aires, Argentina

[4] Consejo Nacional de Investigaciones Científicas y Técnicas (CONICET), Ciudad Autónoma de Buenos Aires, Argentina

[5] Instituto de Química, Universidade Federal Fluminense, Outeiro de São João Batista, 24020-007, Niterói, RJ, Brazil

[6] Instituto de Física, Universidade Federal do Rio de Janeiro, CP68528, 21941-972, Rio de Janeiro, RJ, Brazil.

*Corresponding author: ipolikarpov@ifsc.usp.br

Abstract

Corn cobs (CCs) are abundant xylan-rich agricultural wastes. Here, we compared CCs XOS yields obtained via two different pretreatment routs, alkali and hydrothermal, using a set of recombinant endo- and exo-acting enzymes from GH10 and GH11 families, which have different restrictions for xylan substitutions. Furthermore, impacts of the pretreatments on chemical composition and physical structure of the CCs samples were evaluated. We

demonstrated that alkali pretreatment route rendered 59 mg of XOS per gram of initial biomass, while an overall XOS yield of 115 mg/g was achieved via hydrothermal pretreatment using a combination of GH10 and GH11 enzymes. These results hold a promise of ecologically sustainable enzymatic valorization of CCs via "green" and sustainable XOS production.

Keywords: Corn cobs; xylooligosaccharides; xylanase; xylosidase; hydrothermal pretreatment; alkali pretreatment

1. Introduction

Corn (*Zea mays*) is an abundant feedstock, with a worldwide production of 44.6 billion bushels in 2020-2021. It has multiple industrial applications, including animal feed, ethanol, oil and beverage productions (*World of Corn*, 2021). Corn by-products, such as cobs, husks, hulls and stalks are xylan-rich lignocellulosic materials (Bajpai, 2014), that can be more efficiently utilized to gain additional economic and ecological benefits.

Lignocellulosic biomass is mainly constituted of cellulose, hemicellulose and lignin, which interpose to form a recalcitrant structure (Jing et al., 2019). Hemicelluloses is a heterogeneous group of polysaccharides, which includes glucurono(arabino)xylan (GAX), gluco(galacto)mannan, arabinogalactans, among others (Niklas et al., 2017).

Corn cobs (CCs) hemicellulose primarily consists of acetylated GAX, with around 9% bearing arabinose substitutions and 5% with glucuronic acid decorations, while acetylations occur in almost half of xylosyl residues (Van Dongen et al., 2011). GAX has a linear backbone of 1,4-β-D-xylopyranose (Xylp) units, decorated with α-L-arabinofuranose (Ara*f*) and 4-O-methyl glucuronic acid (MeGlcA) residues at O-2 and/or O-3 positions (Naidu et al., 2018). Xylan partial hydrolysis produces xylooligosaccharides (XOS), which have well described beneficial health-related properties, including prebiotic, antioxidant (Ávila et al., 2020), anticarcinogenic (Qian et al., 2020) and antibiotic activities (Wang et al., 2021).

XOS production often involves two steps: a pretreatment step to disrupt the recalcitrant lignocellulosic complex and partially solubilize xylan and an enzymatic hydrolysis step to obtain short-chain functional XOS (Santibáñez et al., 2021). The alkaline pretreatment is widely used for plant biomass delignification (McIntosh & Vancov, 2010). As consequence of lignin removal, xylan becomes exposed and can then be efficiently enzymatically hydrolyzed (de Freitas et al., 2019). The use of alkaline solutions also promotes removal of the acetyl groups from the hemicellulose (Kim et al., 2016). However, this strategy has to deal with high corrosiveness of alkaline solutions and polluting effluents (Zheng et al., 2014).

By contrast, hydrothermal pretreatment is environmentally friendly and relies on the effects of hot water on lignocellulosics (Mariano et al., 2020). During this process, acetic acid released from the biomass promotes hydrolysis of the xylan glycosidic bonds (Yue et al., 2022), resulting in depolymerization of xylan into xylose and XOS of variable lengths. The main drawback of hydrothermal treatment for XOS production is generation unwanted long-chain XOS. Therefore, autohydrolysis can be more efficiently employed in combination with enzymatic hydrolysis for conversion of long-chain oligomers into short chain XOS (Santibáñez et al., 2021).

Xylan enzymatic hydrolysis can be accomplished using enzymes with various activities, notably endo-1,4-β-xylanases (EC 3.2.1.8), with GH10 and GH11 being the most common xylanase families (Biely et al., 2016; Garron & Henrissat, 2019; Linares-Pasten et al., 2016). GH10 xylanases are restrictive to the decorations at subsite -1 and require two consecutive unsubstituted xylopyranose residues to perform catalysis (Capetti et al., 2021). GH11 xylanases require three undecorated residues to hydrolyze the xylan backbone and do not tolerate substitutions at subsites -1 and +1 (Capetti et al., 2021).

Biochemical characterization of *Paenibacillus xylanivorans* GH10 and GH11

xylanases (*Px*Xyn10A and *Px*Xyn11B) showed their promising potential for XOS production (Ghio et al., 2018). Furthermore, recent studies (Kadowaki et al., 2021) shed light on structural features of exo-acting GH11 xylosidase (MetXyn11) identified from a compost-derived consortium (Evangelista et al., 2019; Mello et al., 2017), which releases xylobiose as the only product. However, whether the combinations of a GH10 xylanase with traditional GH11 endo-xylanase and/or novel exo-acting GH11 xylosidase would benefit XOS production from lignocellulosic materials remain unclear.

Here we set out to investigate XOS production from abundantly available and largely underutilized CCs. We compared alkali and hydrothermal pretreatment routes combined with enzymatic hydrolysis using *Paenibacillus xylanivorans* GH10 and GH11 xylanases and metatranscriptomic GH11 xylosidase, alone and in combinations. We also investigated changes in structure and composition of CCs, introduced by the pretreatments and optimized the enzymes combinations for efficient, sustainable and "green" XOS production.

2. Material and Methods

2.1 Biomass pretreatments

Sodium hydroxide pretreatment was carried out at 121 ºC for 40 minutes in an autoclave. 1g of CCs powder (dry weight) was added to 10 mL of 1% (w/v) NaOH. Next, the mixture was vacuum filtered to separate solids (CC-Alk) from liquid. The solids were milled and stored for further analysis.

Hydrothermal pretreatment was performed in a 1L Parr reactor with 1:10 (w/v) solids in distilled water at 160 ºC, 73 psi for 60 minutes under mechanical stirring. Separation of solid (CC-HT) and liquid (CC-HT-Liq) fractions was accomplished via vacuum filtration. The samples chemical composition before and after pretreatments was determined as

described in Supplementary Material (SM).

2.2 Physical structure of the lignocellulosic biomass

Physical properties of untreated and pretreated CCs were evaluated using X-ray diffraction (XRD), confocal laser scanning microscopy (CLSM) and ^{13}C solid-state nuclear magnetic resonance (ssNMR) as described previously (Rezende et al., 2011).

2.2.1 X-ray diffraction analysis

Crystallinity indices (CrIs) and average crystallite sizes were determined using X-ray diffraction (XRD) technique. CrIs were estimated by Segal empirical method (Segal et al., 1959), whereas average crystallite sizes were calculated from Scherrer equation (Monshi et al., 2012; Scherrer, 1912). XDR was performed at ambient temperature on Rigaku Rotaflex diffractometer model RU200B (Tokyo, Japan) equipped with a graphite monochromator, operated at a tension of 45 kV and a current of 36 mA. Copper X-ray radiation with a wavelength of 1.54 Å was used. 2θ scan range was chosen from 5º to 50º and scanned in steps of 0.05º. The samples were exposed to the radiation for 15 s in each step.

2.2.2 Confocal laser scanning microscopy analysis

Confocal laser scanning microscopy (CLSM) technique was utilized to evaluate changes in lignin distribution in the samples as a result of the applied pretreatments and to obtain information on its molecular arrangements within the cell wall. Lignin autofluorescence emission spectra were measured using Zeiss LSM 780 confocal microscope with a Coherent Chameleon laser (Ti-Sapphire) for two-photons excitation and a Plan-Apochromat objective lens (20x). The samples were excited by two photons at wavelength 800 nm (1.54 eV) which produces optical transitions with an energy of around 3.1 eV (400

nm, ultraviolet region). Pretreated and untreated biomass samples were suspended in water and deposited on the cover slides. The images were obtained on wet samples, which ensures their homogeneous spreading and horizontal deposition on a microscopic glass slide. CLSM images were obtained as an average of three scans. The total number of dots per image was 1024×1024 and the area of each pixel was associated with the optical resolution of the lens resulting in a lateral resolution of about 250300 nm. The color in the spectral images results from an RGB decomposition of the measured spectra for each image pixel in the visible region between 400 and 700 nm. Multivariate statistical analysis was applied to obtain additional information contained in the confocal microscopy spectral images (Pelegrini et al. 2022).

2.2.3 Space-spectral mapping analysis

The spectral space mapping method (Forgy, 1965; Ma et al., 2010) allows the characterization of multispectral images pixel by pixel, and not by region, as conventionally occurs in CLSM analyses. Essentially, the method performs a pre-processing to reduce the acquisition noise by applying a Gaussian filter to each spectrum recorded in each pixel (spectral pixel). Then, all spectral pixels are classified into K clusters by the K-means method (Pellegrini et al., 2022). The K-means method assigns each of the spectral pixels in one of the K clusters based on the similarity of the pixel's spectrum to the average spectrum (centroid) of one of the K clusters. Thus, the space-spectral mapping method enables the spectral characterization of the entire image space efficiently, in addition to contemplating the quantification of the occurrences of each spectral class. Finally, the occurrence rate of each of the K spectral clusters is calculated by the number of spectral pixels assigned in a K cluster divided by the total number of spectral pixels contained by the image. The average K spectra are normalized and graphically arranged in ascending order with reference to the average

spectral wavelength calculated from the intensity-weighted average, which is used as a weight for each corresponding wavelength. This statistical analysis allows to reveal and significantly enhance an informational context contained in the confocal images (Pellegrini et al., 2022).

2.2.4 ^{1}H Time Domain NMR Relaxometry

The samples were dried at 80 ˚C, under 800-mmHg vacuum for 5 hours and then soaked with ultrapure water overnight. An excess of water was removed by centrifugation (Corning® Costar® Spin-X, 0.45 μm, nylon membrane), applying 100 G for 1 min. All measurements were performed on a Bruker Minispec MQ-20 spectrometer, with a 0.5 T magnetic field (^{1}H Larmor frequency of 20 MHz), by using a CPMG (Carr-Purcell-Meiboom-Gill) sequence, with the acquisition of 35,000 echoes of 70 μs and recycle delays of 10 s. To obtain the T_2 distributions, we applied a numerical Inverse Laplace Transform (ILT) procedure (Song, 2013). The contribution of each interstitial scale was obtained by deconvoluting each T_2 distribution with log-gaussian functions. All experiments were carried out in triplicate. The signal intensity was used to measure the volume of water adsorbed by the biomass, applying CPMG decay of 600 μL of water to calibrate the signal. After the measurements, all samples were dried at 40 °C during 5 days and weighted.

2.2.5 ^{13}C solid state Nuclear Magnetic Resonance Spectroscopy

Solid-state NMR spectroscopy experiments were performed in Bruker Avance III spectrometer at frequencies of 100.5 and 400.0 MHz for ^{13}C and ^{1}H, respectively. A 7 mm double resonance magic angle spinning probe with a frequency stability superior to 1 Hz was used. Ramped cross-polarization under magic angle spinning (^{13}C CPMAS) with RF amplitude varying between 80 – 100 % during 1 ms of contact time was used as an excitation

method. Magic angle spinning of 5 kHz was applied with the Total Suppression of Spinning Sideband method (TOSS) and high-power dipolar decoupling of 70 kHz. ^{13}C and ^{1}H 90° pulse durations of 3.5 and 4.0 μs, respectively, were used. All ssNMR measurements were performed using 2 s recycle delays.

2.3 Enzymes three-dimensional structure analysis

3D structure of *Px*Xyn10A was generated using Alphafold (Jumper et al., 2021). Sequence alignments against Protein Data Bank were performed with BLASTp and homologous crystallographic structures complexed with ligands were selected to evaluate protein-ligand interaction. Structures of GH10 xylanases from *Xanthomonas axonopodis* pv. citri str. 306 (PDB 4PN2) and from *Geobacillus stecrothermophilus* (PDB 4PUD) complexed with xylotriose and xylopentaose, respectively, were superimposed with *Px*Xyn10A using PyMOL (https://pymol.org/2/). For visualization of decorations, a xylopyranose residue α-1,3 bound to arabinofuranosyl and α-1,2 bound to glucuronic acid were built with GLYCAM-Web (https://glycam.org/cb/) and then pair fitted to a desired xylopyranose residue of the appropriately placed ligand.

3D structures of *Px*Xyn11B and MetXyn11 were previously determined by Briganti et al. (2021) and by Kadowaki et al. (2021) , respectively (PDB codes 7KV0 and 7L1W). The ligands were modeled within both GH11 enzymes catalytic sites based on crystallographic structure of *Trichoderma reesei* GH11 xylanase complexed with xylohexaose (PDB 4HK8). Since MetXyn11 lacks the -3 subsite, the non-reducing end xylopyranose residue of the xylohexaose was excised, originating xylopentaose.

2.4 Enzymatic hydrolysis

*Px*Xyn10A (WP_053782506.1), *Px*Xyn11B (WP_053781844.1) and MetXyn11 (ATY75129.1), were expressed and purified according to previously stablished protocols

(Evangelista et al., 2019; Ghio et al., 2018; Kadowaki et al., 2021). Specific activity of MetXyn11 xylosidase against xylotetraose was determined by X2 detection using HPAEC after enzymatic reaction at 50ºC. The activity unit (U) was defined as the amount of enzyme that releases 1 µmol of reducing sugar per minute.

To explore possible synergistic effects, the enzymes were applied to substrates in six different GH10+GH11 combinations. Total enzyme concentration in each reaction was 125 µg/mL, and GH10:GH11 concentration ratios were 1:2; 1:1 and 2:1. Enzymes were also applied one at a time in samples that are referred to as 3:0 and 0:3. Control samples without enzyme addition are designated 0:0.

Two milliliter reactions were carried out in 50 mM phosphate buffer pH 6.0, at 50 ºC for 48 hours, using a ThermoMixer® (Kasvi, Brazil) under agitation, in duplicates. Substrate concentrations were 2% (w/v) for solid substrates and 38% (v/v) for liquid substrate. Hydrolysis reactions were interrupted by boiling the samples for 5 minutes. Then, hydrolysates were centrifuged at 13,500 RPM for 5 minutes and the supernatant was collected for HPAEC analysis.

2.5 Analytical methods for XOS quantification

High performance anion exchange chromatography, coupled with amperometric pulsed detection (HPAEC-PAD) is a very sensitive technique, which allows for precise XOS identification and quantification (Santibáñez et al., 2021). Prior to chromatographic analysis, hydrolysates samples were filtered using 0.22 µm filters (Perfectalab, São Paulo, Brazil). HPAEC-PAD was performed with ICS-5000 system equipped with CarboPAC1 column, 250 mm x 2 mm, both from Dionex (Sunnyvale, USA). As gradient of 100 mM sodium hydroxide (buffer A) and 500 mM sodium acetate plus 100 mM sodium hydroxide (buffer B) was

applied. Flux, temperature and time were set to 0.3 mL/min, 30 ºC and 35 minutes, respectively.

Standard calibration curves of xylooligomers (X1-X6, from Sigma-Aldrich, St. Louis, USA) were used to determine XOS concentrations in hydrolysates. For solid substrates, concentrations (*[XOS]*) were converted to XOS yields based on initial mass (Y_{XOS}), using equation 2, in which the concentration of substrate (*[substrate]*) was 2% and Y_{PT} represents solids recovery after pretreatment.

$Y_{XOS} = [XOS] / [substrate] \cdot Y_{PT}$ Eq. (1)

For liquid substrates, XOS yields were determined by equation 3, where *[substrate]* value was set to 38% (v/v). Liquid volume to initial mass ratio was 20 mL/g.

$Y_{XOS} = [XOS]/[substrate] \cdot (total\ liquor\ volume) / (initial\ mass)$ Eq. (2)

3. Results and discussion

3.1 Biomass chemical characterization

Chemical composition of corn cobs before and after pretreatments is given in Table 1.

Table 1. Corn cobs chemical composition of solid fractions (% dry basis) before (CC-*IN*) and after alkali (CC-Alk) or hydrothermal (CC-HT) pretreatments. N/D – Not detected. The experiments were conducted in duplicate.

Component	**CC-*IN* (%)**	**CC-Alk (%)**	**CC-HT (%)**
Glucans	30.3 ± 0.9	47.3 ± 0.4	47 ± 1
Xylan	25.8 ± 0.4	35.2 ± 0.8	18.7 ± 0.2
Arabinose	1.83 ± 0.02	2.51 ± 0.06	1.58 ± 0.08

Acetyl groups	2.80 ± 0.03	N/D	0.82 ± 0.03
Lignin	20 ± 1	8.3 ± 0.5	30 ± 2
Ashes	1.2 ± 0.1	2.1 ± 0.3	0.30 ± 0.04
Extractives	7.5 ± 0.1	-	-
Total	90 ± 3	95 ± 2	99 ± 3

Composition of untreated CCs is in line with the literature (Baptista et al., 2020; Poletto et al., 2020). The xylan fraction in CCs is higher as compared to other xylan-rich feedstocks, such as sugarcane bagasse (Espirito Santo et al., 2018) and wheat straw (Isci et al., 2021), which makes CCs a promising raw material for XOS production. The xylan from studied samples of CCs is 27% acetylated and arabinofuranosyl decorated (around 7%).

As expected, the main effect of alkaline pretreatment on CCs composition was delignification (from original 20% in raw CCs to 8% of lignin in CC-Alk) and simultaneous enrichment in cellulose and xylan fractions. Additionally, alkaline pretreated samples were deacetylated as a result of NaOH neutralization. On the other hand, hydrothermal pretreatment of CCs samples (CC-HT) resulted in a significant reduction in xylan content (27.5%) and only partial deacetylation. HPAEC analysis of liquid fraction has shown that xylan was solubilized and could be found in the form of XOS with various degree of polymerization (Figure 1). Monomeric sugar contents of the liquid fraction were 4.85 g/L xylose, 0.99 g/L glucose, 0.98 g/L arabinose and 0.96 g/L acetic acid.

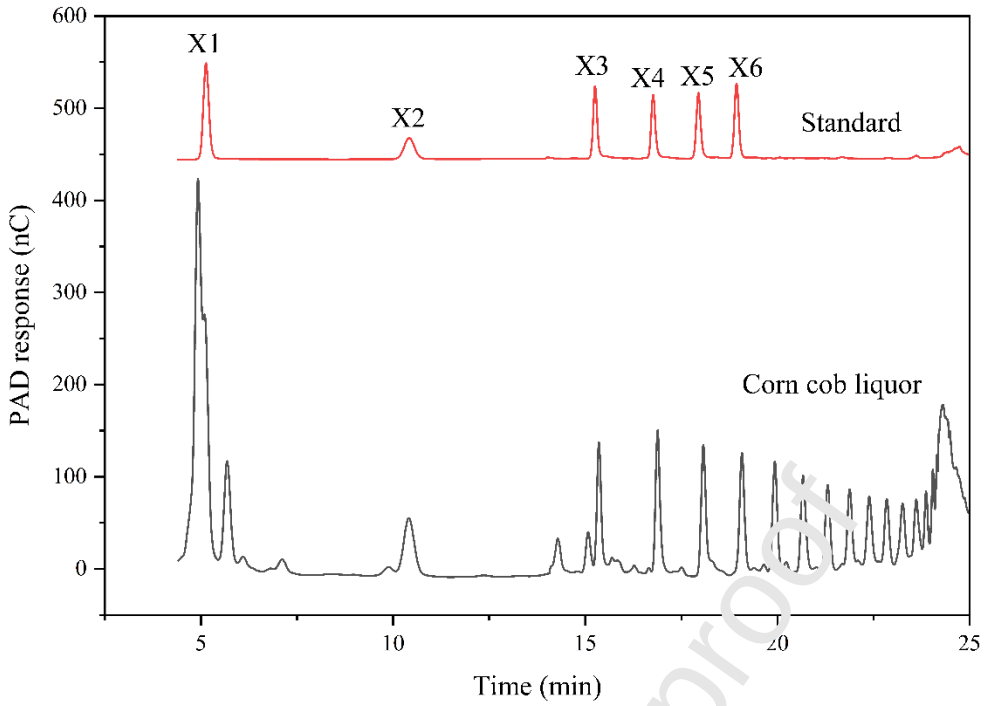

Figure 1. HPAEC profile of corn cob hydrothermal liquor, showing the presence of a wide range of xylooligosaccharides.

3.2 Physical characterization of the biomass

Biomass physical properties such as porosity, cellulose crystallinity and lignin distribution are impacted by pretreatments (Scapini et al., 2021). Such modifications may influence enzymes accessibility to cellulose and xylan, and impact XOS production yields (Zhang et al., 2021).

3.2.1 X-ray diffraction analysis

Cellulose crystallinity might have significant impacts on the efficiency of enzymatic hydrolysis (Espirito Santo et al., 2018; Park et al., 2010). The crystallinity could be significantly altered by the pretreatments of lignocellulosic biomass which is the reason we determined crystallinity indices (CrIs) and the average size of the crystallites of raw and pretreated corn cobs samples using X-ray diffraction (XRD) (Table 2).

The CrIs of pretreated corn cobs samples and the average size of the cellulose

crystallites were significantly different from original, untreated biomass (Table 2). Comparison of chemical composition analysis of CCs samples (Table 1) and their crystallinity indices and average crystallite sizes (Table 2) shows that the changes in CCs crystallinity were primarily due to removal of lignin and hemicellulose fractions, caused by pretreatments. CrIs estimates based on the Segal equation (Table 2) agree well with the decrease in lignin and hemicellulose contents of the pretreated samples (Table 1). Lower CrI values observed for raw bagasse samples are consistent with their higher lignin and/or hemicellulose content as compared with the pretreated samples.

It is known that hemicellulose and lignin removal allow for direct interfacing between cellulose crystallites, enabling co-crystallization that results in larger crystallites and higher crystallinities of the pretreated lignocellulosic biomass samples (Driemeier et al., 2015). This view is consistent with our results (Table 2), which show that the applied pretreatments resulted in higher CrIs and larger crystallites. Both CrIs and the average crystallite sizes were larger for alkaline-pretreated CCs samples, presumably because of the more homogeneous removal of lignin, as demonstrated by CSLM images and their analyses. Hydrothermal pretreatment led to much less homogeneous samples, which possibly resulted in their somewhat smaller CrIs and average crystallite sizes, which nevertheless were considerable higher than that of raw, untreated CCs samples (Table 2).

Table 2. Crystallinity indices and average crystallite sizes. CC: Corn cobs.

Sample	Crystallinity indices[1] (%)	Average cellulose crystallite widths (nm)
Untreated CC	33.9 ± 3.7	3.0 ± 0.7
Alkaline pretreated CC	46.2 ± 2.4	3.6 ± 0.1
Hydrothermally pretreated CC	44.4 ± 4.7	3.2 ± 0.2

[1] Calculated according to the method described by Segal et al. (1959)

3.2.2 Confocal scanning laser microscopy (CSLM) analysis

Confocal scanning laser microscopy (CSLM) using two-photon excitation is a powerful optical technique for visualization of lignin autofluorescence, which reports on lignin distribution and differences in lignin properties in lignocellulosic materials (De Micco & Aronne, 2007; Coletta et al., 2013). Using this technique, it is possible to obtain information on lignin molecular arrangement in plant biomass, such as CCs, for example (Coletta et al., 2013).

Fig.2 shows CSLM images of CCs before and after each of the applied pretreatment. Figs. 2A, 2E and 2I are the raw spectral images of the CCs in which each image pixel is associated to an emission spectrum of lignin at that particular position. Its spectral shape and position can be strongly modified by pretreatments (Coletta et al., 2013; Pellegrini et al., 2022). The color in the images results from an RGB decomposition of the measured spectrum for each image pixel in the visible region between 400 and 700 nm. Therefore, changes in the color of the CCs fragments in the spectral images are necessarily variations in the band shape and/or band shift associated to the change of the original lignin arrangement in the cell walls, due to lignin aggregation or to lignin chemical modification due to pretreatments (Pellegrini et al., 2022). Multivariate statistical classification was applied to the spectral images (Pellegrini et al., 2022) in which the seven most representative spectra were classified and each image pixel was colored with the false color that represents the spectral class in that position (Figs 2B, 2F and 2J). The normalized spectra of the seven spectral classes and their occurrences are depicted in Figs. 2C, G, K and 2D, H, L, respectively. Untreated CCs (Figs. 2-A:D) emit fluorescence predominantly (~80% of the pixels on the CCs samples confocal plane) in the blue range (400 – 500 nm) of electromagnetic spectrum, reflecting homogeneous lignin arrangement and distribution in the cell walls. The red CLASS7

spectrum (less 1% occurrence) is dominated by chlorophyll emission at around 780 nm. Spectral emission of lignin in the hydrothermally pretreated CCs samples (Figs. 2E-H) shifts to a longer wavelength spectral region (yellow-red; 550 – 650 nm, Fig. 2G), with a broader spectral shape that is distributed almost homogenously over the CCs images. Except for the variation in chlorophyll emission at 780 nm, the spectral shape of lignin emission changes very little between the classes in Figure 2F after hydrothermal treatment. These small spectral variations between classes are barely distinguishable in the raw spectral image (Fig. 2E). However, the spectral changes due to the hydrothermal pretreatment are signatures of strong aggregation process that broaden the lignin molecular states toward the visible range and promote excited state migration (energy transfer) and energy relaxation to molecules of low energy (Coletta et al., 2013). As a consequence, a number of the pixels with the lignin autofluorescence in blue spectral regions decreases, whereas significantly higher number of pixels reveal lignin autofluorescence in yellow and red spectral regions. Furthermore, as the confocal image is a planar cut of a round shape sample that contains information of its interior and surface contours, the spectral classification gives an idea of the degree of lignin aggregation in these two regions. Fig. 2F shows that lignin is less aggregated and/or condensed due to the blue shift of the emission inside the CCs samples than in the surface region, where the emission is more redshifted and consistent with more aggregated lignin (Fig. 2-F). This is indicative of partial lignin solubilization, redistribution, condensation and reprecipitation at the surface of CCs particles as well as changes in natural arrangement lignin structure after hydrothermal treatment. The emission of lignin from alkali pretreatment of CCs shifts from the blue-greenish spectral range for the untreated CCs samples to the green spectral region (Figs. 2I-L), indicating changes in the original lignin arrangement brought upon by alkali pretreatment and large lignin solubilization. Although the spectral image (Fig. 2I) is homogeneous in terms of emission, its spectral classification (Fig. 2J) shows further

details of how the lignin is organized within the cell walls. Fig. 2K shows the spectral classes were classified in terms of the broadening process in the emission spectral region of longer wavelengths, consistent with level of aggregation in these samples. This image shows that lignin is less aggregated (smaller broadening for the blue classes) inside the cell wall and more aggregated (higher broadening for the yellow-red classes) in the interface areas between the cell walls, indicating that lignin accumulates in these areas. This is consistent with partial lignin dissolution and removal of lignin particles from the alkaline-pretreated samples (Table 1; Espirito Santo et al., 2018).

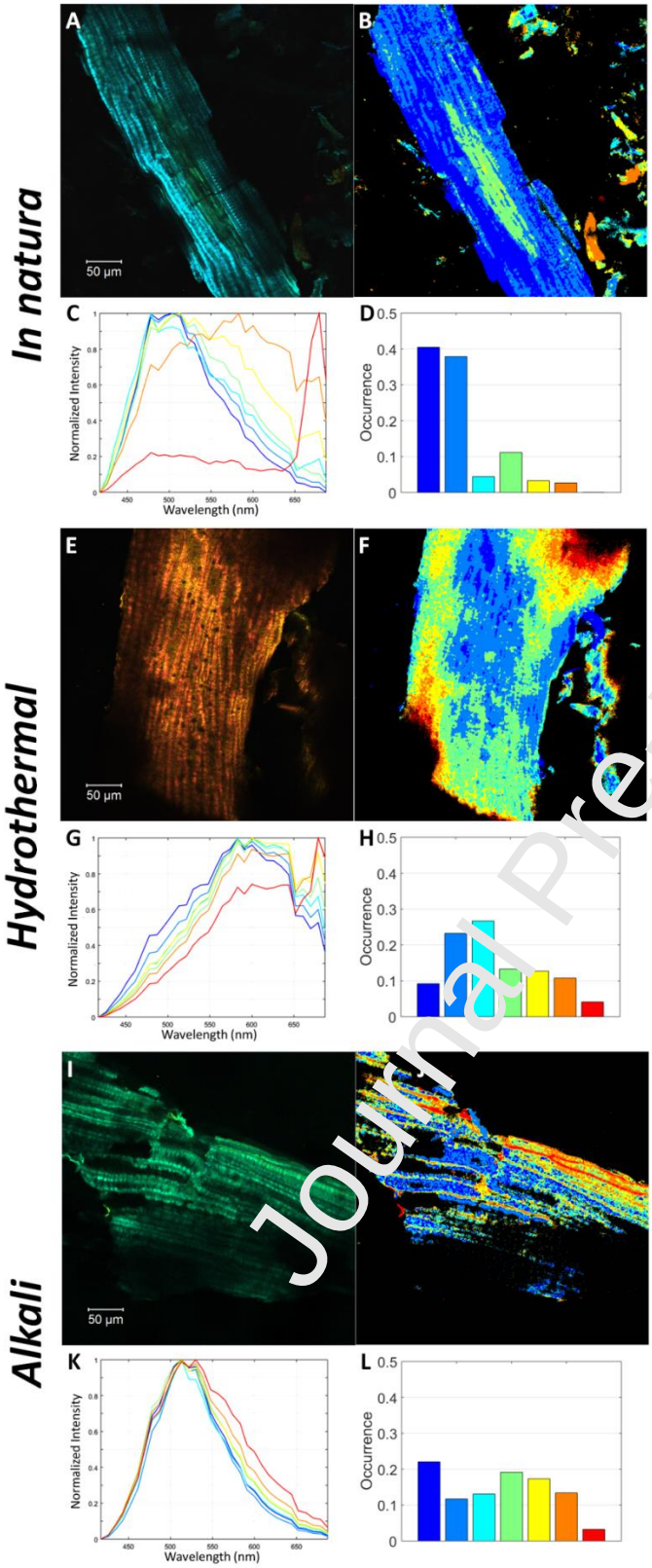

Figure 2. CLSM image of corn cobs samples in a spectral mode. Panes (A-D), (E-H) and (I-L) report on untreated, hydrothermally pretreated and alkali pretreated samples, respectively.

3.2.3 ^{1}H Time Domain NMR Relaxometry

CPMG experiments were used to evaluate the water volume adsorbed by the CCs samples. The adsorbed water volume was determined by comparing the CPMG first echo intensities measured for each water saturated sample with that measured for 600 μL of ultrapure water. The dried masses were measured to obtain the adsorbed volume by mass ratio. Average values of 4.2 ± 0.2 mL/g, 4.2 ± 0.2 mL/g and 4.0 ± 0.1 mL/g were obtained for the raw, alkaline and hydrothermal pretreated samples. Within the errors, all samples revealed similar water adsorption capacity (Table S1; SM). The T_2 distributions reveal three components corresponding to water in pores at the microfibril surfaces (T_2 about 1 ms), water adsorbed within the lignin-hemicellulose matrix on the fiber surface (T_2 ~ 10 ms) and water inside luminal pores T_2 (~ 100 ms) (Meng & Ragauskas, 2014). The relative area of each component for the samples (Figure S1; SM) reflects the quantity of water in each interstitial scale. Compared to original samples, the relative areas associated to the microfibrils and the lignin hemicellulose matrix decrease in the alkaline-pretreated samples and increase for hydrothermally pretreated samples. This reveals an increased hydrophilicity in the more internal interstitial sites in the cell wall of samples submitted to hydrothermal pretreatment (Figure S1, SM).

3.2.4 ^{13}C solid state Nuclear Magnetic Resonance Spectroscopy

^{13}C solid state NMR spectroscopy was used to evaluate the effect of the pretreatments on the composition and/or cellulose microstructure of the CCs samples. The spectra of raw and pretreated CCs are shown in Figure 3, where the geometric markers indicate spectral regions attributed predominantly to hemicelulose (blue circles), lignin (pink stars) and cellulose (orange squares) (detailed signal assignments are given in (Rezende et al., 2011). All spectra were normalized by the signal at 88 ppm (C4-carbon of inner structure of

cellulose microfibrils). Noteworthy, the signals from acetyl groups, at 21 ppm and 172 ppm, vanish and the lignin signals are strongly reduced in CC-Alk samples, while for CC-HT the signals from acetyl groups are reduced while lignin signals remain. This is in agreement with the chemical composition analysis (Table 1).

Detailed inspection of the spectral regions associated to C4 (80-90 ppm) and C6 (60-65 ppm) carbons of the carbohydrate fractions of CC-Alk and CC-HT samples, which are highlighted in the insets of Figure 3, reveals considerable differences in the signal profile around 82.2 ppm. Considering only cellulose chains, the split observed for the C4 carbon signal (80 to 90 ppm) and C6 signal (60 to 65 ppm) is assigned to two distinct conformational environments of cellulose referred to as domain 1 (signals at ~88 ppm and ~65 ppm), and domain 2 (signals at ~84 ppm and 62 ppm). Domain 1 has been attributed to more ordered cellulose chains in the core of the microfibril, sometimes named crystalline cellulose (Foston et al., 2011; Park et al., 2010). As recently proposed (Terrett et al., 2019), it is also expected that domain 1 has some contribution from surface chains which are in more ordered conformation states induced upon the interaction with other cell wall components. Domain 2 is attributed to conformational disordered cellulose chains at the microfibril surfaces which do not interact with other cell wall components, being sometimes referred to as amorphous cellulose (Foston et al., 2011; Park et al., 2010). This is the reason we normalized the spectra by the signal at 88 ppm, which is mostly attributed to internal cellulose chains, so less prone to variation upon the pretreatments, as evidenced by the little variations in the average cellulose crystallite widths obtained by the X-ray diffraction analysis.

Besides the cellulose signals, the spectral regions from 80-90 ppm and 60-65 ppm can also have contributions from C4 and C6 signals of hemicellulose (Dick-Pérez et al., 2011; Wickholm et al., 1998). Furthermore, Dupree and co-workers (Simmons et al., 2016; Terrett et al., 2019) applied extensive 2D NMR characterization of ^{13}C labeled *Arabidopsis thaliana*

samples to demonstrate that signals at 105.2 ppm, 82.2 ppm, 75.2 ppm, 72.3 ppm and 64.3 ppm can be assigned to xylan in flattened two-fold screw conformation bound to the surface of the cellulose microfibril. These signals were also identified in sugar cane bagasse samples, using ^{13}C ssNMR spectra edition associated to multivariate analysis (Espirito Santo et al., 2022). Notably, the signal at 82.2 ppm can be taken as a fingerprint of the xylan in two-fold screw conformation, since other hemicellulose components or conformationally disordered xylan (which assumes three-fold screw conformation) are not expected to have peaks at these positions (Simmons et al., 2016). The difference in C4 carbon signals between CC-Alk and CC-HT, seen around 82.2 ppm in the inset of Figure 3 (dashed line), indicates a significantly higher amount of xylan in flattened two-fold screw conformation retained in the CC-Alk sample. The same conclusion can be drawn from the C6 signal, which depicts higher intensity around 64.3 ppm for the CC-Alk than for CC-HT sample. Of note, despite the strong signal superposition, in all regions where three-fold screw xylan signals are expected to appear (105.2 ppm, 82.2 ppm, 75.2 ppm, 72.3 ppm and 64.3 ppm), the observed signals intensities were considerably higher for CC-Alk samples as compared to CC-HT samples, which further corroborates our hypothesis. Therefore, the differences observed in the C4 and C6 signals in the spectra of the CC-Alk and CC-HT samples can be mostly attributed to the higher amount of xylan in flattened two-fold screw conformation bound to the surface of the cellulose microfibril, which is chiefly retained in the solid fraction after the alkaline pretreatment.

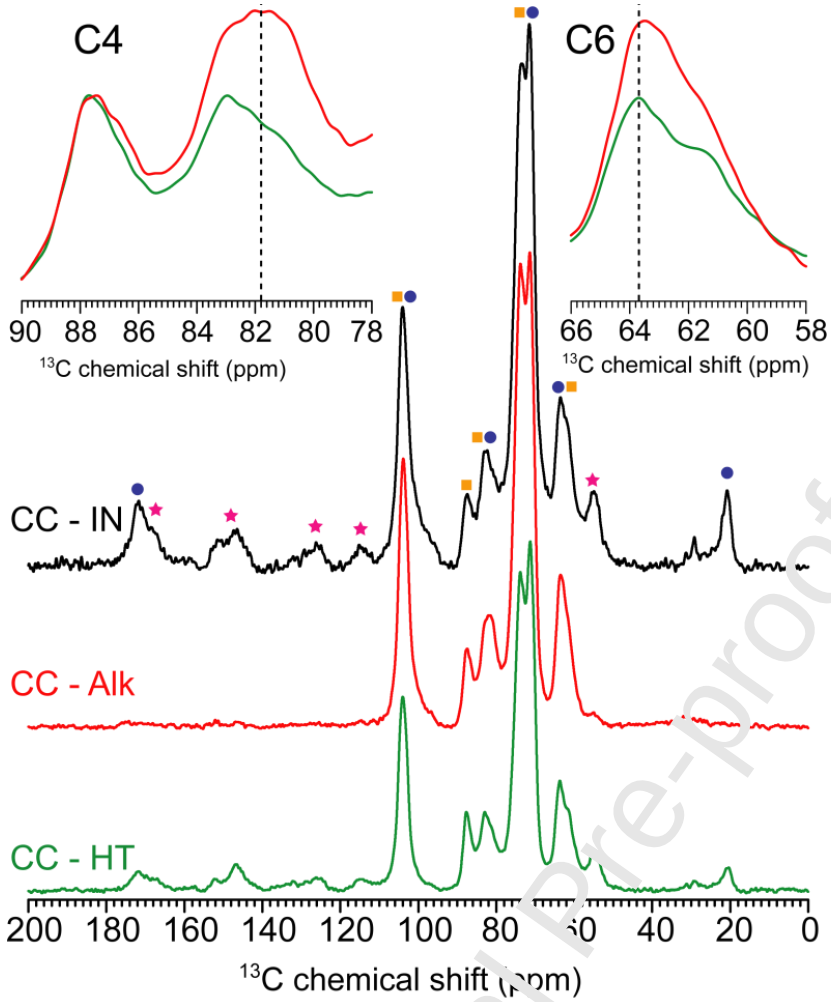

Figure 3. Top: ^{13}C ssNMR spectra of a raw corn cobs samples (CC-IN). Middle: spectra of the corn cobs samples submitted to alkaline treatment (CC-Alk). Bottom: spectra of corn cobs samples submitted to hydrothermal treatment (CC-HT). The insets show zoom in the spectral regions associated to the C4 (80-90 ppm) and C6 (60-65 ppm) carbons of the carbohydrate fractions of CC-Alk and CC-HT samples

It has been shown that cellulose-xylan interactions are stabilized by restraining the 2-fold screw xylan backbone conformation while lying on the cellulose surface (Pereira et al., 2017). It has also been demonstrated that at high temperatures (160 °C), xylan migrates from the hydrophilic to the hydrophobic cellulose surfaces (Pereira et al., 2017). This implies that hydrothermal pretreatments should predominantly eliminate xylan from the hydrophilic

cellulose surface, which is consistent with the NMR results. First, it can explain why two-fold xylan is predominantly retained in the CC-Alk but not in CC-HT samples. Second, the migration of xylan to the hydrophobic cellulose surface due to the hydrothermal pretreatment is consistent with our NMR relaxometry results (Figure S1), which reveals significantly higher amount of water in the interstitial regions related to the cellulose microfibril surfaces and to the lignin-hemicellulose matrix at the surface of the fibers. Kang and coworkers (Kang et al., 2019) have demonstrated that three-fold conformation of xylan involves electrostatic interactions between xylan polar groups (disassociated from cellulose microfibrils) and lignin. Since alkaline pretreatment strongly affects lignin, it is likely to interfere predominantly with the three-fold xylan. On the opposite, hydrothermal pretreatment will preferentially affect cellulose-associated xylan in two-fold screw conformation.

3.3 Three-dimensional structural analysis of the enzymes used for XOS production

To better understand CCs GAX enzymatic degradation, we decided to investigate structural features of the two xylanases and the xylosidase employed in the enzymatic hydrolysis step.

*Px*Xyn10A structure was predicted with Alphafold, with an overall pLDDT of 97.64. Superimposition of *Px*Xyn10A structure with *Geobacillus stearothermophilus* xylanase crystallographic structure complexed with xylopentaose (PDB 4PUD), allowed for identification of all the subsites (from +3 to -2) of the active site. Furthermore, superposition with *Xanthomonas axonopodis* pv citri XynB structure bound to xylotriose (PDB 4PN2) permitted the identification of -3 subsite. Therefore, we were able to build a xylohexaose molecule based on the forementioned ligands, to explore *Px*Xyn10A structure with X6 ligand adequately positioned in the enzyme catalytic cleft.

It is recognized that glycone subsites of GH10 xylanases are often well conserved,

while the aglycone subsites are more prone to variations, leading to different affinities of the branched substrates (Linares-Pasten et al., 2016). Consistent with the previous reports, the ligand interactions with Lys32 and His88 via O3 and with Asn110 and catalytic Glu218 via O2, are present in subsite -1, whereas highly conserved Lys32, Trp251, Glu28 and Asn29 interact with the substrate in subsite -2 (Pell et al., 2004).

In xylan, arabinofuranose decorations can occur both at O2 or O3 positions of xylopyranose residues, while 4-O-methyl-glucuronic acid substitutions are bound to xylopyranose backbone via α-1,2 linkage (Capetti et al., 2021). Considering this, to understand *Px*Xyn10A tolerance to xylan decorations, we analyzed the orientation of each xylopyranose residue O2 and O3 atoms for xylohexaose placed into the catalytic cleft. Subsites +3 and -3 have no steric hindrances for decorations at O2 or O3 positions, indicating that these residues can bear arabinofuranose or 4-O-methyl-glucuronic acid decorations (Fig 4A). At subsites +2 and -1, on the other hand, O2 and O3 are both occluded by enzyme's surface, and therefore, these positions do not tolerate binding of branched substrates. Differently, subsite -2 displays O3 apparently well positioned for substitution, while O2 is sterically impeded, thus *Px*Xyn10A can only tolerate an arabinofuranose decoration at this subsite. Finally, modelling of arabinofuranose at O3 and glucuronic acid at O2 positions in subsite +1 (Supplementary Figure S2) showed that, indeed, both arabinofuranose and glucuronic acid decorations can be accommodated.

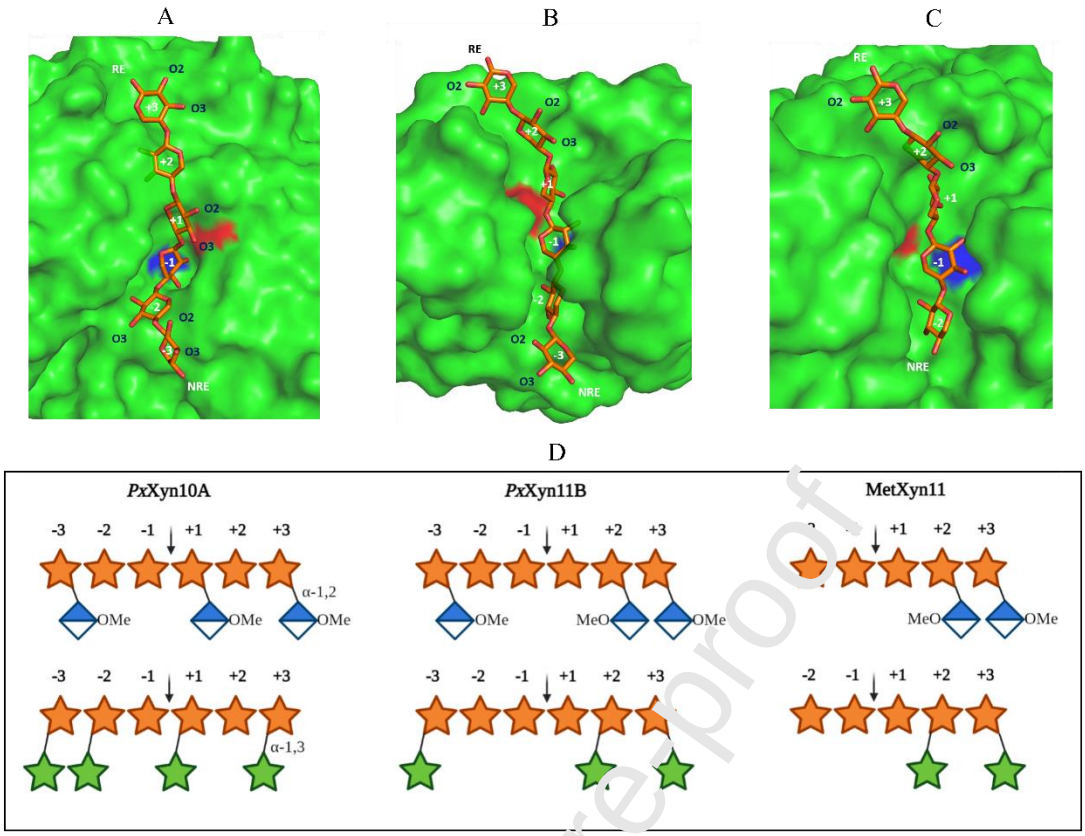

Figure 4. Structural models of *Px*Xyn10A (A), *Px*Xyn11B (B) and MetXyn11 (C) with a xylohexaose (A and B) or xylopentaose (C) molecule modeled in their catalytic clefts. Subsites and oxygens numbers are labeled, as well as the reducing (RE) and the non-reducing ends (NRE). Panel (D) shows a schematic representation of enzymes tolerance to arabinofuranose (shown as green stars) and 4-O-methylglucuronic acid (shown as blue and white diamonds) decorations in each of their subsites. Xylan backbone is shown as golden stars. Blue and red areas on enzyme surface correspond to catalytic Glu218 and Glu111 surfaces, respectively.

*Px*Xyn11B is a *bona fide* GH11 endo-xylanase. Analysis of its structure with a xylohexaose molecule in the catalytic site shows that subsites -2, -1 and +1 hold ligand O2 and O3 atoms facing towards enzymes surface, being impeded to bear decorations, while subsites -3, +2 and +3 arrangements are favorable to accept arabinose or glucuronic acid

decorations (Figure 4B) (Briganti et al., 2021). Finally, MetXyn11 is an exo-acting GH11 xylosidase. Its main structural difference to traditional GH11 xylanases consists in two additional loops (9 and 13), which occlude subsite -3 and enclose the exit of the catalytic cleft. This results in xylobiose being the only product this enzyme can generate (Kadowaki et al., 2021). A study on MetXyn11 structure with X6 reveals that all but subsites +2 and +3 are sterically impeded for xylan decorations (Figure 4C) (Kadowaki et al., 2021).

Altogether, our results confirm that *Px*Xyn10A follows the tolerance pattern observed in other GH10 xylanases with well conserved the glycone subsites (Linares-Pasten et al., 2016), while being rather arabinose-permissive in the aglycone subsites, with the only restriction being subsite +2. Comparison of enzymes tolerances to branching (Figure 4D) indicates that *Px*Xyn10A might perform better on more substituted substrates in comparison to GH11 counterparts.

3.4 Enzymatic XOS production

Enzymatic hydrolysis was carried out using two endo-xylanases, *Px*Xyn11B and *Px*Xyn10A from GH11 and GH10 families, respectively and GH11 exo-xylosidase MetXyn11 on liquid and solid substrates obtained after hydrothermal and alkaline pretreatments. The substrates present either xylan accessible after lignocellulosic complex disruption (CC-Alk, CC-HT), or soluble high-DP XOS (CC-HT-Liq).

The specific enzymatic activities of xylanases *Px*Xyn10A and *Px*Xyn11B have been previously determined as 99.58 ± 0.14 U/mg and 131.56 ± 0.08 U/mg using wheat arabinoxylan as a substrate (Ghio et al., 2018). Specific activity of xylosidase MetXyn11 against xylotetraose was experimentally determined in present study and found equal to 158 ± 4 U/mg.

Enzymatic hydrolysis of alkali pretreated CCs xylan revealed that combinations of

*Px*Xyn11B with *Px*Xyn10A performed better than any of these enzymes used alone. This shows that differences in permissibility of GH10 and GH11 xylanases to xylan decorations is important for degradation of insoluble substrates (CC-Alk). Furthermore, the absence of acetylations allows for efficient contribution of traditional GH11 endo-xylanase for XOS production. Chromatographic profiles of CC-Alk enzymatic hydrolysis products present several peaks with retention times greater than that of xylohexaose, which probably correspond to branched arabino-xylooligosaccharides (AXOS) (Supplementary Figure S3). Application of the exo-acting xylosidase MetXyn11 alone resulted in only small amounts of XOS from the solid fraction of alkali-pretreated CCs. This is consistent with the molecular mechanism of MetXyn11 action, which allows hydrolysis of non-decorated X2 from non-reducing ends of xylan chain until when the enzyme encounters decoration. After this molecular event, MetXyn11 stalls and dissociates from the xylan chain. This results in relatively inefficient xylan degradation (Fig. 5A).

Similar limited activity of MetXyn11 is observed in hydrolysis of solids from hydrothermally pretreated CCs (Fig. 5B). Interestingly, a different effect was observed for the combination *Px*Xyn10A + *Px*Xyn11B, in which the use of GH10 alone resulted the best yields of short XOS. This difference is probably due to the fact that xylan from hydrothermal pretreatment is still partially acetylated, as demonstrated by the composition analysis (Table 1). In addition to decorations, acetyl groups are known to provide hindrances for xylan enzymatic hydrolysis, especially for the enzymes from GH11 family, impairing enzymes access to xylan backbone (Hu & Saddler, 2018). Furthermore, xylan from solid fraction of hydrothermally pretreated CCs has slightly higher amount of arabinose decorations than alkali pretreated xylan (8.4% vs 7.1%, respectively). It becomes clear that higher GH10 loads led to improved XOS yields from acetylated and more branched substrates, because of better tolerance of the enzymes toward decorations and acetylation.

Enzymatic hydrolysis of CCs hydrothermal liquor resulted in the highest yields of short undecorated XOS. In this fraction, xylan is solubilized and fragmented in a wide range of decorated and undecorated XOS with different DP and MetXyn11 was remarkably more active against longer XOS. MetXyn11+PxXyn10A were able to efficiently convert soluble xylooligomers into short functional XOS, especially xylobiose and xylotriose, known for their enhanced prebiotic activity (Vázquez et al., 2000). On the opposite, enzymatic hydrolysis of the liquid fraction after alkaline pretreatment did not render significant amount of XOS, presumably because of unproductive binding of xylanases on lignin which shields the small fraction of co-solubilized xylan.

Comparing XOS yields obtained by two different routes, the alkali route for XOS production resulted in up to 59 ± 2 mg of short undecorated XOS per gram of initial biomass, obtained after hydrolysis with combination of *Px*Xyn10A with *Px*Xyn11B at 2:1 ratio, while hydrothermal pretreatment rendered up to 41 ± 1 mg/g from the solid fraction when hydrolyzed in that same enzymatic condition (Figure 5A&B). Although XOS production was 1.4 times higher for alkali pretreated CCs, it is noteworthy that xylan concentration in these samples is almost two times higher as compared to the samples after hydrothermal pretreatment (Table 1), revealing smaller efficiency of enzymatic XOS production from alkali-pretreated CCs. In addition, 73.5 ± 0.2 mg/g of XOS were produced from the liquid fraction of hydrothermal pretreatment for the most efficient GH10 + GH11 combination, which was *Px*Xyn10A + MetXyn11 at 1:1 ratio in this case (Figure 5C). Combining the highest yields of solid and liquid fractions of hydrothermal pretreatment, a total yield was 114.5 ± 1.2 mg/g of XOS. Yields calculated in terms of xylan available in the original biomass can be found in Table 3.

Table 3. A summary of XOS yields obtained after enzymatic hydrolysis including calculation

based on initial biomass and based on available xylan. 1 gram of initial biomass contains 0,258 gram of xylan.

Pretreatment strategy	**Most efficient enzymatic combination**	**Yield (mg XOS / g of initial biomass)**		**Yield (mg XOS / g of xylan)**	
Alkali	*Px*Xyn10A + *Px*Xyn11B (2:1)	59 ± 2		228 ± 23	
Hydrothermal (Solid)	*Px*Xyn10A + *Px*Xyn11B (2:1)	41 ± 1	114.5 ± 1.2	159 ± 4	444 ± 5
Hydrothermal (Liquor)	*Px*Xyn10A + MetXyn11 (1:1)	73.5 ± 0.2		284.9 ± 0.8	

For comparison, using a more severe alkali pretreatment, with 5% KOH at 90°C for 1h, and a commercial GH10 xylanase, Boonchuay et al. (2018) obtained 79 mg/g of XOS (excluding xylose). Furthermore, Teng et al. (2010) produced 102 mg/g of XOS from CCs after steam explosion pretreatment at 196ºC for 5 minutes. These results indicate that hydrothermal pretreatment followed by enzymatic hydrolysis of CCs is an efficient way to obtain short functional XOS. Furthermore, it is a green and sustainable technology which does not require utilization of potentially polluting chemicals.

XOS health related properties have been vastly characterized in the recent years and their consolidated use as food additive justify the assessment of XOS production routes through efficient methodologies, such as enzymatic technology. We have been able to produce a mixture of XOS from pretreated CCs samples comprising mainly short non-substituted XOS as well as decorated XOS (Supplementary Figure S3). Gut microbiota has differential preferences for linear and substituted XOS depending on bacteria species. For instance, while prebiotic effect on *Bifidobacterium adolescentis* can be observed both with linear and decorated XOS (Vacilotto et al., 2022), *Lactobacillus brevis* selective growth can only be achieved with non-substituted XOS (Nordberg Karlsson et al., 2018). Similarly, it has

been demonstrated that antioxidant activity is also impacted by structural features of XOS molecules (Bouiche et al., 2020). Indeed, higher DP XOS obtained from glucuronoxylan had improved antioxidant capability as compared to arabino-XOS (Bouiche et al., 2020).

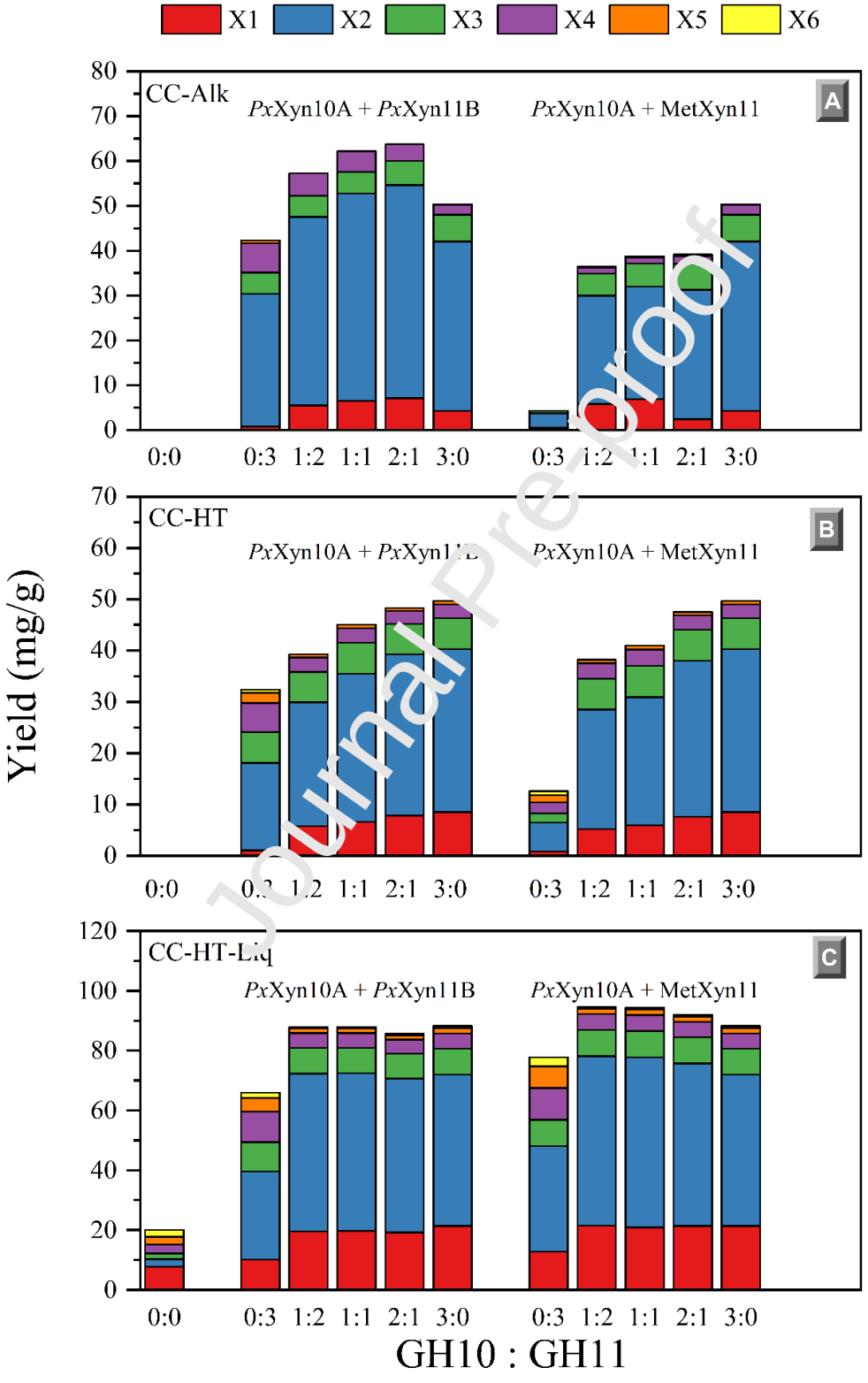

Figure 5. XOS yields from enzymatic hydrolysis. (A) alkali pretreated CCs; (B) solid fraction from hydrothermally pretreated CCs; (C) liquid fraction of hydrothermally pretreated CCs. 0:0 represent control samples, with no enzyme addition. 3:0 and 0:3 represent samples hydrolyzed with only GH11 and GH10 enzymes, respectively.

4. Conclusions

Here, we analyzed the impacts of two pretreatments on chemical composition and physical structure of CCs during enzymatic XOS production, revealing the differences in the impacts of hydrothermal and alkaline pretreatments. Notably we showed that xylan in two-fold conformation associated with the cellulose surface is predominant in the alkaline pretreated samples, whereas hydrothermal pretreatment causes migration of xylan to hydrophobic surfaces of cellulose and has smaller effects on xylan in three-fold conformation. We demonstrated the advantages of performing enzymatic hydrolysis on hydrothermally pretreated CCs, which yielded almost two-times more short-chain XOS. Furthermore, this route is ecologically friendlier, since xylan depolymerization relies only on hot water. Moreover, we analyzed structural basis of *Px*Xyn10A tolerance to xylan decorations, which turns it into an efficient enzymatic tool for prebiotic xylooligosaccharides production.

Conflict of interest

None

Funding

This research was supported by Fundação de Amparo à Pesquisa do Estado de São Paulo (FAPESP) via grants 2019/10942-0 (to CC) and 15/13684-0 (to IP) and by the Conselho Nacional de Desenvolvimento Científico e Tecnológico (CNPq, grant 303988/2016-9).

References

Ávila, P. F., Martins, M., de Almeida Costa, F. A., & Goldbeck, R. (2020). Xylooligosaccharides production by commercial enzyme mixture from agricultural wastes and their prebiotic and antioxidant potential. *Bioactive Carbohydrates and Dietary Fibre*, *24*(August), 1–9. https://doi.org/10.1016/j.bcdf.2020.100234

Bajpai, P. (2014). Xylan: Occurrence and Structure. *Xylanolytic Enzymes*, *may 1997*, 9–18. https://doi.org/10.1016/b978-0-12-801020-4.00002-0

Baptista, S. L., Carvalho, L. C., Romaní, A., & Domingues, L. (2020). Development of a sustainable bioprocess based on green technologies for xylitol production from corn cob. *Industrial Crops and Products*, *156*, 112867. https://doi.org/10.1016/J.INDCROP.2020.112867

Boonchuay, P., Techapun, C., Leksawasdi, N., Seesuriyachan, P., Hanmoungjai, P., Watanabe, M., Takenaka, S., & Chaiyaso, T. (2018). An integrated process for xylooligosaccharide and bioethanol production from corncob. *Bioresource Technology*, *256*, 399–407. https://doi.org/10.1016/j.biortech.2018.02.004

Borgia, G. C., Brown, R. J. S., & Fantazzini, P. (1998). Uniform-Penalty Inversion of Multiexponential Decay Data. *Journal of Magnetic Resonance*, *132*(1), 65–77. https://doi.org/10.1006/jmre.1998.1387

Bouiche, C., Boucherba, N., Benallaoua, S., Martinez, J., Diaz, P., Pastor, F. I. J., & Valenzuela, S. V. (2020). Differential antioxidant activity of glucuronoxylooligosaccharides (UXOS) and arabinoxylooligosaccharides (AXOS) produced by two novel xylanases. *International Journal of Biological Macromolecules*, *155*, 1075–1083. https://doi.org/10.1016/J.IJBIOMAC.2019.11.073

Briganti, L., Capetti, C., Pellegrini, V. O. A., Ghio, S., Campos, E., Nascimento, A. S., & Polikarpov, I. (2021). Structural and molecular dynamics investigations of ligand

stabilization via secondary binding site interactions in Paenibacillus xylanivorans GH11 xylanase. *Computational and Structural Biotechnology Journal*, *19*, 1557–1566. https://doi.org/10.1016/j.csbj.2021.03.002

Capetti, C. C. de M., Vacilotto, M. M., Dabul, A. N. G., Sepulchro, A. G. V., Pellegrini, V. O. A., & Polikarpov, I. (2021). Recent advances in the enzymatic production and applications of xylooligosaccharides. *World Journal of Microbiology and Biotechnology 2021 37:10*, *37*(10), 1–12. https://doi.org/10.1007/S11274-021-03139-7

Coletta, V. C., Rezende, C. A., da Conceição, F. R., Polikarpov, I., & Guimarães, F. E. G. (2013). Mapping the lignin distribution in pretreated sugarcane bagasse by confocal and fluorescence lifetime imaging microscopy. *Biotechnology for Biofuels*, *6*(1), 43. https://doi.org/10.1186/1754-6834-6-43

de Freitas, C., Carmona, E., & Brienzo, M. (2019). Xylooligosaccharides production process from lignocellulosic biomass and bioactive effects. *Bioactive Carbohydrates and Dietary Fibre*, *18*, 100184. https://doi.org/10.1016/j.bcdf.2019.100184

De Micco, V., & Aronne, G. (2007). Combined histochemistry and autofluorescence for identifying lignin distribution in cell walls. *Biotechnic & Histochemistry*, *82*(4–5), 209–216. https://doi.org/10.1080/10520290701713981

Driemeier, C., Mendes, F. M., Santucci, B. S., & Pimenta, M. T. B. (2015). Cellulose co-crystallization and related phenomena occurring in hydrothermal treatment of sugarcane bagasse. *Cellulose*, *22*(4), 2183–2195. https://doi.org/10.1007/s10570-015-0638-7

Espirito Santo, M., Rezende, C. A., Bernardinelli, O. D., Pereira, N., Curvelo, A. A. S., deAzevedo, E. R., Guimarães, F. E. G., & Polikarpov, I. (2018). Structural and compositional changes in sugarcane bagasse subjected to hydrothermal and organosolv pretreatments and their impacts on enzymatic hydrolysis. *Industrial Crops and Products*, *113*(January), 64–74. https://doi.org/10.1016/j.indcrop.2018.01.014

Evangelista, D. E., de Oliveira Arnoldi Pellegrini, V., Santo, M. E., McQueen-Mason, S., Bruce, N. C., & Polikarpov, I. (2019). Biochemical characterization and low-resolution SAXS shape of a novel GH11 exo-1,4-β-xylanase identified in a microbial consortium. *Applied Microbiology and Biotechnology*, *103*(19), 8035–8049. https://doi.org/10.1007/s00253-019-10033-8

Forgy, E. W. (1965). Cluster analysis of multivariate data - Efficiency vs interpretability of classifications. *Biometrics*, *21*(3), 768.

Garron, M. L., & Henrissat, B. (2019). The continuing expansion of CAZymes and their families. *Current Opinion in Chemical Biology*, *53*, 82–87. https://doi.org/10.1016/j.cbpa.2019.08.004

Ghio, S., Ontañon, O., Piccinni, F. E., Marrero Díaz de Villegas, R., Talia, P., Grasso, D. H., & Campos, E. (2018). Paenibacillus sp. A59 GH10 and GH11 Extracellular Endoxylanases: Application in Biomass Bioconversion. *Bioenergy Research*, *11*(1), 174–190. https://doi.org/10.1007/s12155-017-9887-7

Hu, J., & Saddler, J. N. (2018). Why does GH10 xylanase have better performance than GH11 xylanase for the deconstruction of pretreated biomass? *Biomass and Bioenergy*, *110*(January), 13–16. https://doi.org/10.1016/j.biombioe.2018.01.007

Isci, A., Thieme, N., Lamp, A., Zverlov, V., & Kaltschmitt, M. (2021). Production of xylo-oligosaccharides from wheat straw using microwave assisted deep eutectic solvent pretreatment. *Industrial Crops and Products*, *164*, 113393. https://doi.org/10.1016/J.INDCROP.2021.113393

Jing, Y., Guo, Y., Xia, Q., Liu, X., & Wang, Y. (2019). Catalytic Production of Value-Added Chemicals and Liquid Fuels from Lignocellulosic Biomass. *Chem*, *5*(10), 2520–2546. https://doi.org/10.1016/J.CHEMPR.2019.05.022

Jumper, J., Evans, R., Pritzel, A., Green, T., Figurnov, M., Ronneberger, O.,

Tunyasuvunakool, K., Bates, R., Žídek, A., Potapenko, A., Bridgland, A., Meyer, C., Kohl, S. A. A., Ballard, A. J., Cowie, A., Romera-Paredes, B., Nikolov, S., Jain, R., Adler, J., … Hassabis, D. (2021). Highly accurate protein structure prediction with AlphaFold. *Nature 2021 596:7873*, *596*(7873), 583–589. https://doi.org/10.1038/s41586-021-03819-2

Kadowaki, M. A. S., Briganti, L., Evangelista, D. E., Echevarría-Poza, A., Tryfona, T., Pellegrini, V. O. A., Nakayama, D. G., Dupree, P., & Polikarpov, I. (2021). Unlocking the structural features for the xylobiohydrolase activity of an unusual GH11 member identified in a compost-derived consortium. *Biotechnology and Bioengineering*, *118*(10), 4052–4064. https://doi.org/10.1002/bit.27860

Kang, X., Kirui, A., Dickwella Widanage, M. C., Mentink-Vigier, F., Cosgrove, D. J., & Wang, T. (2019). Lignin-polysaccharide interactions in plant secondary cell walls revealed by solid-state NMR. *Nature Communications*, *10*(1), 347. https://doi.org/10.1038/s41467-018-08252-0

Kim, J. S., Lee, Y. Y., & Kim, T. H. (2016). A review on alkaline pretreatment technology for bioconversion of lignocellulosic biomass. *Bioresource Technology*, *199*, 42–48. https://doi.org/10.1016/J.BIORTECH.2015.08.085

Linares-Pasten, J. A., Aronsson, A., & Karlsson, E. N. (2016). Structural Considerations on the Use of Endo-Xylanases for the Production of prebiotic Xylooligosaccharides from Biomass. *Current Protein & Peptide Science*, *19*(1), 48–67. https://doi.org/10.2174/1389203717666160923155209

Ma, L., Crawford, M. M., & Tian, J. (2010). Local Manifold Learning-Based k -Nearest-Neighbor for Hyperspectral Image Classification. *IEEE Transactions on Geoscience and Remote Sensing*. https://doi.org/10.1109/TGRS.2010.2055876

Mariano, A. P. B., Unpaprom, Y., & Ramaraj, R. (2020). Hydrothermal pretreatment and acid

hydrolysis of coconut pulp residue for fermentable sugar production. *Food and Bioproducts Processing*, *122*, 31–40. https://doi.org/10.1016/J.FBP.2020.04.003

McIntosh, S., & Vancov, T. (2010). Enhanced enzyme saccharification of Sorghum bicolor straw using dilute alkali pretreatment. *Bioresource Technology*, *101*(17), 6718–6727. https://doi.org/10.1016/J.BIORTECH.2010.03.116

Mello, B. L., Alessi, A. M., Riaño-Pachón, D. M., DeAzevedo, E. R., Guimarães, F. E. G., Espirito Santo, M. C., McQueen-Mason, S., Bruce, N. C., & Polikarpov, I. (2017). Targeted metatranscriptomics of compost-derived consortia reveals a GH11 exerting an unusual exo-1,4-β-xylanase activity. *Biotechnology for Biofuels*, *10*(1), 254. https://doi.org/10.1186/s13068-017-0944-4

Meng, X., & Ragauskas, A. J. (2014). Recent advances in understanding the role of cellulose accessibility in enzymatic hydrolysis of lignocellulosic substrates. *Current Opinion in Biotechnology*, *27*, 150–158. https://doi.org/10.1016/j.copbio.2014.01.014

Monshi, A., Foroughi, M. R., & Monshi, M. R. (2012). Modified Scherrer Equation to Estimate More Accurately Nano-Crystallite Size Using XRD. *World Journal of Nano Science and Engineering*, *02*(03), 154–160. https://doi.org/10.4236/wjnse.2012.23020

Naidu, D. S., Hlangothi, S. P., & John, M. J. (2018). Bio-based products from xylan: A review. *Carbohydrate Polymers*, *179*(May 2017), 28–41. https://doi.org/10.1016/j.carbpol.2017.09.064

Niklas, K. J., Cobb, E. D., & Matas, A. J. (2017). The evolution of hydrophobic cell wall biopolymers: from algae to angiosperms. *Journal of Experimental Botany*, *68*(19), 5261–5269. https://doi.org/10.1093/jxb/erx215

Nordberg Karlsson, E., Schmitz, E., Linares-Pastén, J. A., & Adlercreutz, P. (2018). Endo-xylanases as tools for production of substituted xylooligosaccharides with prebiotic properties. In *Applied Microbiology and Biotechnology* (Vol. 102, Issue 21, pp. 9081–

9088). https://doi.org/10.1007/s00253-018-9343-4

Park, S., Baker, J. O., Himmel, M. E., Parilla, P. A., & Johnson, D. K. (2010). Cellulose crystallinity index: measurement techniques and their impact on interpreting cellulase performance. *Biotechnology for Biofuels*, *3*(1), 10. https://doi.org/10.1186/1754-6834-3-10

Pell, G., Taylor, E. J., Gloster, T. M., Turkenburg, J. P., Fontes, C. M. G. A., Ferreira, L. M. A., Nagy, T., Clark, S. J., Davies, G. J., & Gilbert, H. J. (2004). The Mechanisms by Which Family 10 Glycoside Hydrolases Bind Decorated Substrates. *Journal of Biological Chemistry*, *279*(10), 9597–9605. https://doi.org/10.1074/jbc.M312278200

Pellegrini, V. de O. A., Ratti, R. P., Filgueiras, J. G., Falvo, M., Coral, M. A. L., Guimaraes, F. E. G., DeAzevedo, E. R., & Polikarpov, I. (2022). Differences in chemical composition and physical properties caused by industrial storage on sugarcane bagasse result in its efficient enzymatic hydrolysis. *Sustainable Energy & Fuels*, *6*(2), 329–348. https://doi.org/10.1039/D1SE01243A

Pereira, C. S., Silveira, R. L., Dupree, P., & Skaf, M. S. (2017). Effects of Xylan Side-Chain Substitutions on Xylan–Cellulose Interactions and Implications for Thermal Pretreatment of Cellulosic Biomass. *Biomacromolecules*, *18*(4), 1311–1321. https://doi.org/10.1021/acs.biomac.7b00067

Poletto, P., Pereira, G. N., Monteiro, C. R. M., Pereira, M. A. F., Bordignon, S. E., & de Oliveira, D. (2020). Xylooligosaccharides: Transforming the lignocellulosic biomasses into valuable 5-carbon sugar prebiotics. *Process Biochemistry*, *91*(December 2019), 352–363. https://doi.org/10.1016/j.procbio.2020.01.005

Provencher, S. W. (1982). CONTIN: A general purpose constrained regularization program for inverting noisy linear algebraic and integral equations. *Computer Physics Communications*, *27*(3), 229–242. https://doi.org/10.1016/0010-4655(82)90174-6

Qian, S., Zhou, J., Chen, X., Ji, W., Zhang, L., Hu, W., & Lu, Z. (2020). Evaluation of an efficient fed-batch enzymatic hydrolysis strategy to improve production of functional xylooligosaccharides from maize straws. *Industrial Crops and Products*, *157*(August), 112920. https://doi.org/10.1016/j.indcrop.2020.112920

Rezende, C., de Lima, M., Maziero, P., DeAzevedo, E., Garcia, W., & Polikarpov, I. (2011). Chemical and morphological characterization of sugarcane bagasse submitted to a delignification process for enhanced enzymatic digestibility. *Biotechnology for Biofuels*, *4*(1), 54. https://doi.org/10.1186/1754-6834-4-54

Santibáñez, L., Henríquez, C., Corro-Tejeda, R., Bernal, S., Armijo, B., & Salazar, O. (2021). Xylooligosaccharides from lignocellulosic biomass: A comprehensive review. *Carbohydrate Polymers*, *251*(September 2020), 117118. https://doi.org/10.1016/j.carbpol.2020.117118

Scapini, T., dos Santos, M. S. N., Bonatto, C., Wancura, J. H. C., Mulinari, J., Camargo, A. F., Klanovicz, N., Zabot, G. L., Tres, M. V., Fongaro, G., & Treichel, H. (2021). Hydrothermal pretreatment of lignocellulosic biomass for hemicellulose recovery. *Bioresource Technology*, *342*, 126033. https://doi.org/10.1016/J.BIORTECH.2021.126033

Scherrer, P. (1912). Bestimmung der inneren Struktur und der Größe von Kolloidteilchen mittels Röntgenstrahlen. In *Kolloidchemie Ein Lehrbuch* (pp. 387–409). Springer Berlin Heidelberg. https://doi.org/10.1007/978-3-662-33915-2_7

Segal, L., Creely, J. J., Martin, A. E., & Conrad, C. M. (1959a). An Empirical Method for Estimating the Degree of Crystallinity of Native Cellulose Using the X-Ray Diffractometer. *Textile Research Journal*, *29*(10), 786–794. https://doi.org/10.1177/004051755902901003

Segal, L., Creely, J. J., Martin, A. E., & Conrad, C. M. (1959b). An Empirical Method for

Estimating the Degree of Crystallinity of Native Cellulose Using the X-Ray Diffractometer. *Textile Research Journal*, *29*(10), 786–794. https://doi.org/10.1177/004051755902901003

Simmons, T. J., Mortimer, J. C., Bernardinelli, O. D., Pöppler, A.-C., Brown, S. P., DeAzevedo, E. R., Dupree, R., & Dupree, P. (2016). Folding of xylan onto cellulose fibrils in plant cell walls revealed by solid-state NMR. *Nature Communications*, *7*(1), 13902. https://doi.org/10.1038/ncomms13902

Teng, C., Yan, Q., Jiang, Z., Fan, G., & Shi, B. (2010). Production of xylooligosaccharides from the steam explosion liquor of corncobs coupled with enzymatic hydrolysis using a thermostable xylanase. *Bioresource Technology*, *101*(19), 7679–7682. https://doi.org/10.1016/J.BIORTECH.2010.05.004

Terrett, O. M., Lyczakowski, J. J., Yu, L., Iuga, D., Franks, W. T., Brown, S. P., Dupree, R., & Dupree, P. (2019). Molecular architecture of softwood revealed by solid-state NMR. *Nature Communications*, *10*(1), 4978. https://doi.org/10.1038/s41467-019-12979-9

Tsuchida, J. E., Rezende, C. A., De Oliveira-Silva, R., Lima, M. A., D'Eurydice, M. N., Polikarpov, I., & Bonagamba, T. J. (2014). Nuclear magnetic resonance investigation of water accessibility in cellulose of pretreated sugarcane bagasse. *Biotechnology for Biofuels*, *7*, 127. https://doi.org/10.1186/s13068-014-0127-5

Vacilotto, M. M., Pellegrini, V. O. A., Sepulchro, A. G. V., Capetti, C. C. d. M., Curvelo, A. A. S., Marcondes, W. F., Arantes, V., & Polikarpov, I. (2022). Paludibacter propionicigenes GH10 xylanase as a tool for enzymatic xylooligosaccharides production from heteroxylans. *Carbohydrate Polymers*, *275*, 118684. https://doi.org/10.1016/j.carbpol.2021.118684

Van Dongen, F. E. M., Van Eylen, D., & Kabel, M. A. (2011). Characterization of substituents in xylans from corn cobs and stover. *Carbohydrate Polymers*, *86*(2), 722–

731. https://doi.org/10.1016/J.CARBPOL.2011.05.007

Vázquez, M. J., Alonso, J. L., Domínguez, H., & Parajó, J. C. (2000). Xylooligosaccharides: Manufacture and applications. *Trends in Food Science and Technology*, *11*(11), 387–393. https://doi.org/10.1016/S0924-2244(01)00031-0

Wang, Q., Wang, X. F., Xing, T., Li, J. L., Zhu, X. D., Zhang, L., & Gao, F. (2021). The combined impact of xylo-oligosaccharides and gamma-irradiated Astragalus polysaccharides on growth performance and intestinal mucosal barrier function of broilers. *Poultry Science*, *100*(3), 100909. https://doi.org/10.1016/j.psj.2020.11.075

World of corn. (2021). National Corn Growers Association. https://www.worldofcorn.com/

Yue, P., Hu, Y., Tian, R., Bian, J., & Peng, F. (2022). Hydrothermal pretreatment for the production of oligosaccharides: A review. *Bioresource Technology*, *343*, 126075. https://doi.org/10.1016/J.BIORTECH.2021.126075

Zhang, H., Han, L., & Dong, H. (2021). An insight to pretreatment, enzyme adsorption and enzymatic hydrolysis of lignocellulosic biomass: Experimental and modeling studies. *Renewable and Sustainable Energy Reviews*, *140*, 110758. https://doi.org/10.1016/J.RSER.2021.110758

Zheng, Y., Zhao, J., Xu, F., & Li, Y. (2014). Pretreatment of lignocellulosic biomass for enhanced biogas production. *Progress in Energy and Combustion Science*, *42*(1), 35–53. https://doi.org/10.1016/J.PECS.2014.01.001

Credit Author Statement

Caio Cesar de Mello Capetti: Data curation, Formal analysis, Investigation, Validation, Writing - original draft, Writing - review & editing. **Vanessa O. Arnoldi Pellegrini**: Data curation, Formal analysis, Investigation, Validation, Writing - original draft, Writing - review & editing. **Melissa Cristina do Espirito Santo:** Data curation, Formal analysis, Investigation, Validation. **Anelyse Abreu Cortez:** Data curation, Formal analysis, Investigation, Validation. **Maurício Falvo:** Data curation, Formal analysis, Investigation, Validation, Methodology, Writing - original draft. **Antonio Arrigo da Silva Curvelo**: Data curation, Formal analysis, Investigation, Validation, Writing - original draft. **Eleonora Campos**: Data curation, Formal analysis, Investigation, Validation, Writing - original draft. **Jefferson Gonçalves Filgueiras**: Data curation, Formal analysis, Investigation, Validation, Methodology, Writing - original draft, Writing - review & editing. **Francisco E.G. Guimaraes:** Conceptualization, Formal analysis, Investigation, Validation, Methodology, Writing - original draft, Writing - review & editing. **Eduardo R. deAzevedo:** Data curation, Formal analysis, Investigation, Validation, Methodology, Writing - original draft, Writing - review & editing. **Igor Polikarpov:** Conceptualization, Resources, Formal analysis, Investigation, Validation, Methodology, Supervision, Writing - original draft, Writing - review & editing.

Declaration of interests

☒ The authors declare that they have no known competing financial interests or personal relationships that could have appeared to influence the work reported in this paper.

☐The authors declare the following financial interests/personal relationships which may be considered as potential competing interests:

Graphical abstract